A PDF-Based Model for Boundary Layer Clouds. Part II: Model Results

JEAN-CHRISTOPHE GOLAZ

Department of Atmospheric Science, Colorado State University, Fort Collins, Colorado

VINCENT E. LARSON

Atmospheric Science Group. Department of Mathematical Sciences, University of Wisconsin–Milwaukee, Milwaukee, Wisconsin

WILLIAM R. COTTON

Department of Atmospheric Science, Colorado State University, Fort Collins, Colorado

(Manuscript received 14 November 2001, in final form 28 May 2002)

ABSTRACT

A new single-column model for the cloudy boundary layer, described in a companion paper, is tested for a variety of regimes. To represent the subgrid-scale variability, the model uses a joint probability density function (PDF) of vertical velocity, temperature, and moisture content. Results from four different cases are presented and contrasted with large eddy simulations (LES). The cases include a clear convective layer based on the Wangara experiment, a trade wind cumulus layer from the Barbados Oceanographic and Meteorological Experiment (BOMEX), a case of cumulus clouds over land, and a nocturnal marine stratocumulus boundary layer.

Results from the Wangara experiment show that the model is capable of realistically predicting the diurnal growth of a dry convective layer. Compared to the LES, the layer produced is slightly less well mixed and entrainment is somewhat slower. The cloud cover in the cloudy cases varied widely, ranging from a few percent cloud cover to nearly overcast. In each of the cloudy cases, the parameterization predicted cloud fractions that agree reasonably well with the LES. Typically, cloud fraction values tended to be somewhat smaller in the parameterization, and cloud bases and tops were slightly underestimated. Liquid water content was generally within 40% of the LES-predicted values for a range of values spanning almost two orders of magnitude. This was accomplished without the use of any case-specific adjustments.

1. Introduction

In a companion paper (Golaz et al. 2002, hereafter Part I), we described a new boundary layer cloud single-column model (SCM). The model represents the subgrid-scale variability of vertical velocity, temperature, and moisture by use of a joint probability density function (PDF). The PDF is selected from a predetermined family for each grid box and time step, thereby allowing the PDF to vary in space and evolve in time. The family of PDFs employed is the three-dimensional analytic double Gaussian 1 family proposed by Larson et al. (2002). This family was tested against aircraft measurements and output from large eddy simulation (LES) models.

The family of PDFs retained depends on a number of free parameters. They are determined from the mean values of the vertical velocity (w), the liquid water potential temperature (θ_l), the total water specific humidity (q_t), the second-order moments of each as well as the third-order moment of the vertical velocity. Filtered moment equations are integrated in space and time to yield the evolution of these moments. Cloud fraction, liquid water, and higher-order turbulent moments are in turn diagnosed directly from the predicted PDF.

This paper focuses on presenting results from four different boundary layer regimes. They consist of a clear convective layer, a trade wind cumulus layer, a continental cumulus layer, and a stratocumulus-topped boundary layer. The clear boundary layer is based on data collected during the Wangara experiment. The three cloudy cases are all based on the Global Energy and Water Experiment (GEWEX) Cloud Study System (GCSS) boundary layer cloud intercomparison workshops. These cases were chosen because, taken together, they span a very large range of cloud fraction and liquid water values. Each case is simulated with the parameterization as well as an LES model in order to allow for a detailed comparison of the turbulence statistics.

Corresponding author address: Jean-Christophe Golaz, Naval Research Laboratory, Marine Meteorology Division, 7 Grace Hopper Ave., Stop 2, Monterey, CA 93943-5502.
E-mail: golaz@nrlmry.navy.mil

The parameterization is identically configured for each simulation, and no case-specific adjustments are performed.

The LES model used is the Regional Atmospheric Modeling System (RAMS; Pielke et al. 1992; Cotton et al. 2002). It is nonhydrostatic and compressible. Periodic boundary conditions are used in the horizontal directions. The subgrid-scale fluxes are computed following Deardorff (1980) using a prognostic equation for the subgrid-scale turbulence kinetic energy. Condensation is accounted for by a nonprecipitating saturation adjustment scheme in which cloud water is diagnosed using the difference between total water and saturation mixing ratio. The RAMS simulations were compared with previously published simulations to ensure that RAMS agreed well with other LES models. All LES results are horizontally averaged over the domain when compared with the SCM.

When available, we do also compare the SCM with a suite of other LES models to illustrate the variability that arises from one LES model to another. We do so by using LES results of GCSS intercomparison workshop participants. We present these results on the figures as a hatched area which is centered around the mean and whose width is given by twice the standard deviation.

Although we do compare the SCM with observational data from the Wangara field experiment, we compare the parameterization mostly with numerical simulations. We have chosen to do so for several reasons. First, we want to test the SCM using data whose forcings, initial conditions, and boundary conditions are identical to the LES simulations. This eliminates initialization and forcing uncertainties from the evaluation of the performance of the SCM. Second, we want to compare the SCM with vertical profiles of higher-order moments, which are difficult to obtain from observational data. Third, we want to focus specifically on the parameterization's ability to predict turbulence statistics and cloud water, while excluding complications such as precipitation and land surface inhomogeneities. We can accomplish this by using GCSS intercomparison cases, which were specifically designed to be used as test beds for parameterizations. These simulations are based loosely on observed cases and therefore simulate realistic scenarios.

This paper is organized as follows. In the next three sections, we show comparisons of the turbulence statistics between the parameterization and the LES. A brief comparison of the clear convective layer is given, with more emphasis put on the cloudy cases. Section 6 shows results from some sensitivity experiments on the vertical grid spacing. We conclude by summarizing strengths and weaknesses of the new parameterization and discussing future plans.

2. Wangara

Data from the Wangara experiment (Clarke et al. 1971) are used to test the SCM for the case of a clear convective boundary layer. We choose day 33 of the field experiment, which has been selected by many prior authors (e.g., Deardorff 1974; André et al. 1978; Lappen and Randall 2001b) because there were clear skies and little horizontal heat and moisture advection. The RAMS LES and SCM are initialized with profiles of horizontal winds, potential temperature, and water vapor specific humidity measured on 16 August 1967 at 0900 LST, approximately 2 h after sunrise. We simulate 8 h of turbulence evolution in order to capture the daytime growth of the boundary layer. Surface sensible and latent heat fluxes are prescribed as functions of time as in André et al. (1978):

$$\overline{w'\theta'}(t) = 0.18 \cos\left(\frac{t - 45\,000}{36\,000}\pi\right) \text{K m s}^{-1}, \quad (1)$$

$$\overline{w'q_t'}(t) = 1.3 \times 10^{-4}\overline{w'\theta'}(t) \text{ m s}^{-1}, \quad (2)$$

where t is in seconds from 0000 LST on 16 August 1967. No radiation is imposed. Details of the simulation setup are given in Table 1.

Figure 1 depicts the observed profiles of the potential temperature along with the RAMS LES and the SCM results at various times. The mixed-layer potential temperature differs between the LES and observations by only a fraction of a degree, both at 1200 and 1500 LST. The mixed-layer top is almost identical at 1200 LST but is too high in the LES at later times. Deardorff (1974) observed a similar difference and attributed it to a possible overestimation of the surface fluxes and the lack of imposed large-scale vertical motion. Boundary layer growth in the parameterization differs only in minor ways from the LES. The SCM tends to produce a convective layer that is less well mixed than the LES and that has a smaller entrainment rate. At 1500 LST, the top of the boundary layer is located near 1300 m for the parameterization, compared to 1400 m in the LES. The inversion capping the top of the convective layer is also slightly less sharp in the SCM than the LES.

The entrainment rate is physically linked to the magnitude of the heat flux at the top of the convective layer. Because the surface flux is prescribed, the heat flux is essentially the same between the SCM and the LES throughout most of the boundary layer, but differs in the entrainment zone, where the LES produces a more negative flux (Fig. 2a). The minimum values are -32 for the LES and -20 W m^{-2} for the SCM. The ratios of the heat flux at the top of the mixed layer to the surface values are -0.22 and -0.14, respectively. Compared to the generally accepted value of -0.2, the smaller SCM ratio is another indication of the lower entrainment rate. A look at the LES and SCM heat flux budgets (not shown) reveals that the probable cause for this difference is the smaller buoyancy term ($\overline{\theta_l'\theta_v'}$) in the SCM compared to the LES. This is the case because the temperature variance ($\overline{\theta_l'^2}$) is itself smaller than in the LES.

It is well recognized that in the upper half of a con-

TABLE 1. Model setup and forcings for the Wangara experiment.

Model attribute	Forcing
Surface heat fluxes	Prescribed, Eqs. (1) and (2)
Radiative cooling	None
Large-scale advection	None
Large-scale subsidence	None
Surface pressure	1023 (hPa)
Start of simulation	0900 LST 16 Aug 1967
Length of simulation	8 h
SCM:	
Time step	Main time step: 12 s; nested time step: 2 s
Grid spacing	$\Delta z = 40$ m
Domain size	$N_z = 50$
LES:	
Time step	$\Delta t = 2$ s
Grid spacing	$\Delta x = \Delta y = 100$ m; $\Delta z = 40$ m
Domain size	$N_x = N_y = 53$; $N_z = 50$
Case reference	Clarke et al. (1971); Deardorff (1974)

vective boundary layer, the heat flux is generally positive and the temperature lapse rate slightly stable, implying that the heat flux is countergradient (e.g., Deardorff 1966). Parameterizations that utilize a local downgradient closure for the fluxes cannot capture the proper sign of the potential temperature gradient in the upper part of a convective layer. This has frequently been regarded as a shortcoming of these local schemes (e.g., Stull 1988; Ebert et al. 1989). Both the LES and SCM simulations of the Wangara day 33 (Figs. 1b,c) produce a slightly stable lapse rate in the upper part of the boundary layer, indicating that the parameterization is capable of producing a countergradient heat flux. However, the SCM profile is not as well mixed as the LES, possibly due to smaller values of vertical velocity variance.

The vertical velocity variance ($\overline{w'^2}$) is depicted in Fig. 2b. The LES has a maximum variance of 1.5 $m^2\ s^{-2}$ at a height of 500 m, whereas the SCM exhibits a smaller maximum value of 1.1 $m^2\ s^{-2}$ located at a lower height, around 200 m above ground. Also shown is the mixed-layer scaling proposed by Lenschow et al. (1980):

$$\overline{w'^2}/w_*^2 = 1.8(z/z_i)^{2/3}(1 - 0.8z/z_i)^2, \qquad (3)$$

where w_* is the convective velocity scale and z_i the mixed layer depth. These values are $w_* = 1.78$ m s^{-1} and $z_i = 1350$ m for the data shown in Fig. 2b. The agreement between the scaled velocity variance given by (3) and the LES variance is good. The agreement with the SCM is less satisfying, the two main deficiencies of the SCM being that $\overline{w'^2}$ is underestimated in magnitude and peaks too low in the mixed layer. Three terms dominate the budget for $\overline{w'^2}$: buoyancy production, turbulent transport and dissipation. The buoyancy production term follows the heat flux (Fig. 2a). The turbulent transport term has a similar shape, but with a slightly smaller magnitude in the SCM. The biggest difference is the dissipation term, which is generally too large and tends to decrease more with height in the SCM

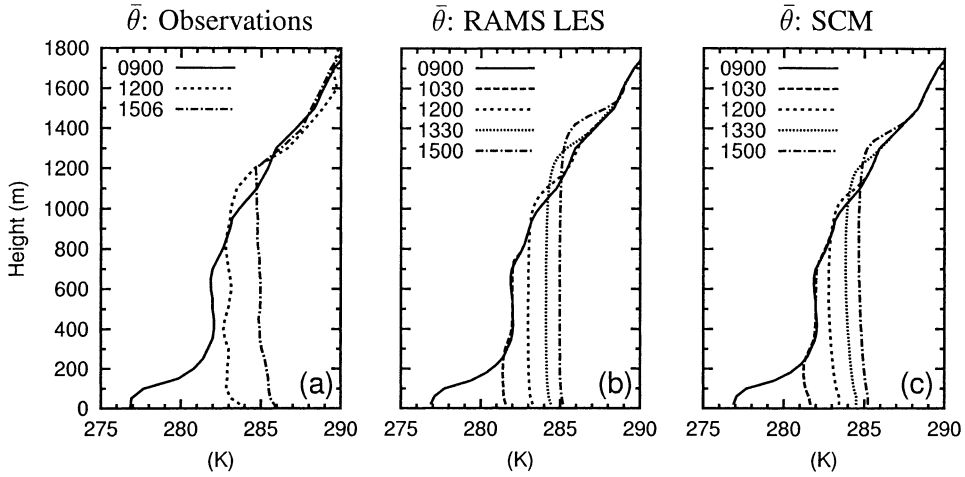

FIG. 1. Profiles of potential temperature observed during (a) the Wangara day 33, and simulated by (b) the RAMS LES and (c) the SCM.

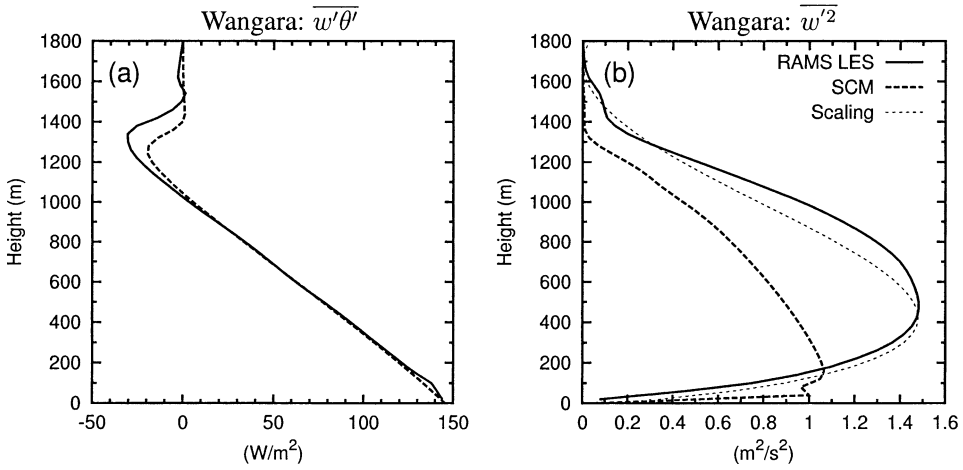

FIG. 2. Comparison of (a) heat flux and (b) vertical velocity variance between the RAMS LES and the SCM; averaged between 1400 and 1500 LST of the Wangara day 33 experiment. RAMS LES results are shown in thick solid lines and SCM in thick dashed lines. The thin dashed line in (b) is the mixed-layer scaling proposed by Lenschow et al. (1980).

than in the LES. The shape of the eddy mixing length is a likely cause of this difference and therefore by extension of the difference between the LES and SCM $\overline{w'^2}$ profiles.

Overall, the simulation of day 33 of the Wangara experiment shows that the SCM is capable of simulating the time evolution of a dry convective boundary layer reasonably well. The main differences are a slightly lower entrainment rate and a less well-mixed layer in the SCM, as compared to the LES.

3. Trade wind cumulus

The trade wind cumulus simulation is derived from the Barbados Oceanographic and Meteorological Experiment (BOMEX), which took place on 22–30 June 1969 (Holland and Rasmusson 1973). The simulation setup is based on the fourth GCSS boundary layer clouds intercomparison workshop. The RAMS LES and the SCM were both initialized with identical profiles of horizontal winds, temperature, and moisture. They were run for 6 h. Details of the experiment setup are given in Table 2. A complete specification of the case and comparison of the results produced by numerous cloud resolving models can be found in Siebesma et al. (2002, manuscript submitted to *Bull. Amer. Meteor. Soc.*, hereafter SIE). The RAMS LES results presented here used a newer version of RAMS that corrected the problems mentioned in SIE. The newer simulation shows considerably less temporal variations in all the fields. The profile of $\overline{w'^2}$ in the subcloud layer is also now in good agreement with the other LES models. Results presented are averaged over the last 3 h of the simulation, unless denoted otherwise explicitly.

Figures 3a,b show the initial profiles of θ_l and q_t, as well as the RAMS LES and SCM outputs. The initial temperature profile consists of the three layers typically found in trade wind cumuli: a mixed layer from the

TABLE 2. Model setup and forcings for BOMEX.

Model attribute	Forcing
Surface heat fluxes	$\overline{w'\theta'} = 8 \times 10^{-3}$ (K m s^{-1}), $\overline{w'q_t'} = 5.2 \times 10^{-2}$ (m s^{-1}).
Radiative cooling	Prescribed as a function of height
Large-scale advection	Prescribed as a function of height
Large-scale subsidence	Imposed
Surface pressure	1015 (hPa)
Length of simulation	6 h
SCM:	
Time step	Main time step: 20 s; nested time step: 4 s
Grid spacing	$\Delta z = 40$ m
Domain size	$N_z = 75$
LES:	
Time step	$\Delta t = 1.5$ s
Grid spacing	$\Delta x = \Delta y = 100$ m; $\Delta z = 40$ m
Domain size	$N_x = N_y = 64$; $N_z = 75$
Case reference	SIE

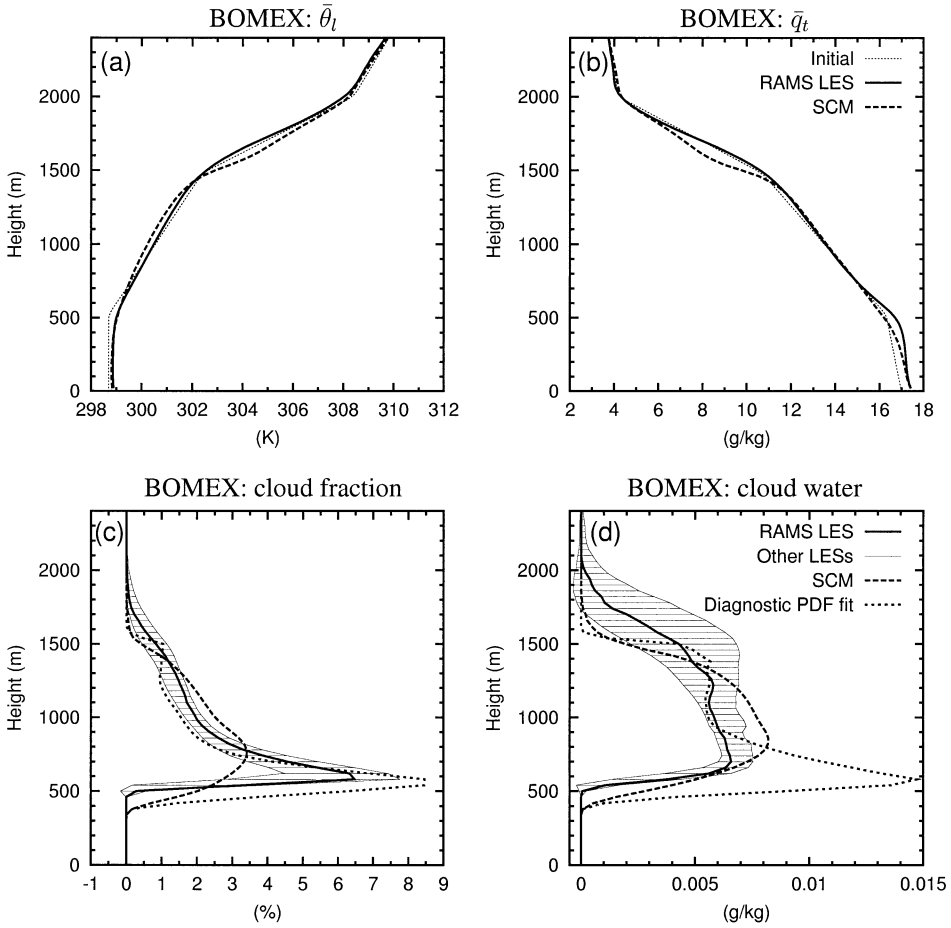

FIG. 3. Mean profiles of (a) liquid water potential temperature, (b) total water specific humidity, (c) cloud fraction, and (d) liquid water for BOMEX. Thick solid lines represent RAMS LES results and thick dashed lines represent SCM results, both averaged over the last 3 h of the simulation. Thin dotted lines in (a) and (b) represent initial profiles; thick dotted lines in (c) and (d) show cloud properties obtained using a diagnostic PDF fit to the RAMS LES data. The hatched regions in (c) and (d) represent twice the standard deviation around the mean of a suite of other LES models (SIE).

surface up to 500 m, a conditionally unstable layer from 500 to 1500 m, and a stable layer between 1500 and 2000 m (Siebesma and Cuijpers 1995). The LES mean profiles obtained after 6 h of simulation are almost identical to the initial conditions, reflecting a near steady-state regime. The intercomparison case was designed so that the surface fluxes are balanced by the vertically integrated large-scale forcings. Profiles from the SCM are very similar to those of the LES. The mixed layer q_t profile is not as well mixed as in the LES, but θ_l is identical in this layer. The moisture gradient in the conditionally unstable layer between 600 and 1500 m is well preserved by the SCM, but the temperature lapse rate becomes a little bit more unstable. Larger differences are observed in the stable layer. The SCM tends to alter the strength of this layer as evidenced by the θ_l and q_t differences between 1500 and 1800 m. Nevertheless, the parameterization is capable of maintaining the three-layer structure of the trade wind cumulus atmosphere throughout the duration of the simulation.

Cloud profiles are depicted in Figs. 3c,d. The RAMS LES produces maximum cloud fraction and liquid water values near cloud base, with profiles decreasing with height. This is typical of a layer average over an ensemble of cumulus clouds where there is a relatively large number of shallow clouds with only a few clouds reaching the domain maximum cloud top. Even though individual cumulus have liquid water profiles that increase with height in their core (e.g., Stevens et al. 2001; SIE), the averaged cloud water profile decreases with height due to the predominance of smaller clouds. The SCM, whose predictive equations are intended to model layer averages, is capable of representing the average decrease in cloud fraction and liquid water with height. The maximum cloud fraction produced by the RAMS LES is approximately 6% at cloud base. Although the

SCM also exhibits a maximum near cloud base, it is smaller (3.5%). In the upper portion of the cloud, between 800 and 1500 m, the SCM slightly overestimates cloud amount. Small differences in cloud base and cloud top are also noticeable. The parameterization underestimates cloud base by approximately 100 m, and cloud top by a larger amount. Results from the GCSS intercomparison workshop showed that many parameterizations had difficulty simulating the low cloud fraction of this trade-wind cumulus case (C.-L. Lappen 2001, personal communication).

Similar trends are apparent in the liquid water profiles (Fig. 3d). In the main part of the cloud layer, between 600 and 1500 m, the parameterization generates approximately 30% more liquid water than the RAMS LES, but underestimates the amount of condensate higher up as a result of the warmer and drier profiles. The LES liquid water path (LWP) is 5.9 g m^{-2} and the SCM is 7.4 g m^{-2}. One should note, however, that the total layer-averaged amount of liquid water is extremely small, in large part due to the low cloud fraction. Parameterizations typically have difficulties predicting such low amounts of condensate. For instance, results presented at the GCSS intercomparison show that the LES models predict a maximum cloud water amount of about 0.006 g kg^{-1}, whereas one-dimensional parameterizations obtained between 0.02 and 1 g kg^{-1} (details available online at http://www.knmi.nl/~siebesma/gcss/bomex.html). Lappen and Randall (2001a) obtain a cloud water profile that varies between 0.02 and 0.05 g kg^{-1}.

The SCM cloud fraction and cloud water are diagnosed using the joint subgrid-scale PDF. The PDF is selected from the underlying family of PDFs based on the values of the turbulent moments (Golaz et al. 2002). The differences between the LES and SCM cloud properties can therefore be a result of two different factors: (i) the SCM and LES moments may differ; or (ii) even if the SCM and LES moments coincide, the assumed shape of the SCM PDF may differ from the LES PDF, leading to differences in the SCM-diagnosed cloud fraction, liquid water, and higher-order moments. Of course, a feedback loop can develop between these two factors in which errors in the shape of the assumed PDF can lead to errors in the prognosed moments at later times. The first factor, the limitations of the family of PDFs, can be tested by simply applying the PDF closure *diagnostically* to the LES-predicted moments to obtain cloud properties. The resulting cloud fraction and liquid water are depicted in Figs. 3c,d with dotted lines. These profiles exhibit lower cloud base and cloud top, similarly to the SCM. This indicates that the underestimation of cloud base and top by the parameterization is largely a result of the family of PDFs. The shape of the cloud fraction produced by the PDF fit is closer to the LES cloud fraction than it is to the SCM, and so is the liquid water, except in the lowest part of the cloud where the PDF fit significantly overestimates cloud water. Differences between SCM and LES cloud amount thus appear to result from a combination of factors (i) and (ii).

Now we examine how close the LES and SCM moments are. Second- and third-order moments of the vertical velocity ($\overline{w'^2}$, $\overline{w'^3}$) are shown in Figs. 4a,b. The RAMS LES $\overline{w'^2}$ has two regions of maximum values, one in the subcloud layer near 200 m and one within the upper part of the cloud layer between 1000 and 1800 m. Between the two, $\overline{w'^2}$ minimizes near cloud base. The subcloud layer has a structure similar to a dry convective layer and similarity theory can be applied there (SIE). The $\overline{w'^2}$ structure is typical of cumulus boundary layers. The SCM produces a similar profile with maxima in the subcloud and cloud layers, and a minimum at cloud base. However, the SCM $\overline{w'^2}$ is approximately 30% larger than in the RAMS LES within the lowest 1400 m of the boundary layer. This may reflect the fact that the eddy mixing length causes the dissipation term to be slightly too weak in the SCM. Here, $\overline{w'^2}$ extends higher in the LES, likely due to higher cloud tops and wave activity in the stable layer above the clouds. Even though the lower cloud tops are partly due to the family of PDFs, the absence of liquid water in the upper part of the domain feeds back into the turbulent moments due to the lack of condensational heating. The $\overline{w'^3}$ obtained by the RAMS LES and the SCM are similar. Both exhibit a maximum in the upper part of the cloud layer and a local minimum near cloud base, although it is not nearly as pronounced in the SCM. The general increase in $\overline{w'^3}$ throughout the cloud layer indicates that the core updrafts become narrower and more vigorous with height. This is to be expected. The area occupied by updrafts becomes narrower because only a fraction of the cumulus clouds extend to the domain maximum cloud top. They become more vigorous because the vertical velocity in the cloud core increases with height (e.g., Siebesma and Cuijpers 1995).

The buoyancy flux ($\overline{w'\theta'_v}$, Fig. 4c) decreases linearly in the subcloud layer, reaching a minimum near cloud base. It increases again in the cloud layer due to the contribution of the liquid water flux. Because buoyancy generates turbulence, the cloud-base $\overline{w'\theta'_v}$ minimum is collocated with the $\overline{w'^2}$ minimum and so are the maxima of $\overline{w'\theta'_v}$ and $\overline{w'^2}$ in the cloud. The RAMS LES and SCM fluxes are comparable, with the major difference in the upper part of the domain. Because the SCM produces shallower clouds, it does not generate any liquid water flux above 1600 m, in contrast to the LES. For the total water fluxes (Fig. 4d), the LES exhibits a moderately negative gradient from the surface up to 1300 m, indicating a slight moistening of this layer, topped by a larger gradient between 1300 to 1900 m, where most of the surface moisture ventilated by the clouds is deposited. The SCM flux is generally comparable, with two notable exceptions. The gradient of the water flux reverses sign between 400 and 700 m and 1600 and 1900 m, reflecting a drying of these two layers. Not

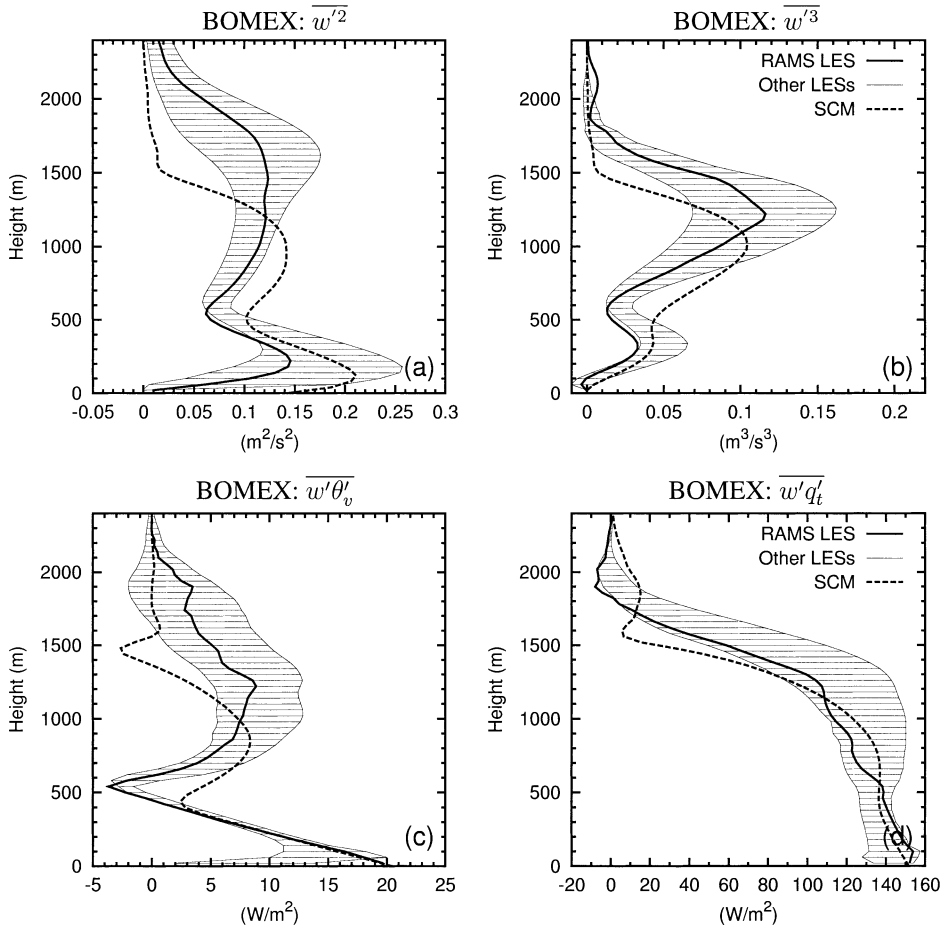

FIG. 4. Profiles of (a) $\overline{w'^2}$, (b) $\overline{w'^3}$, (c) $\overline{w'\theta'_v}$, and (d) $\overline{w'q'_t}$ averaged over the last 3 h of the BOMEX simulation. Solid lines are RAMS LES results and dashed lines are SCM outputs. The hatched regions represent twice the standard deviation around the mean of a suite of other LES models (SIE).

surprisingly, these layers are where the mean humidity profile of the SCM defers the most from the LES (Fig. 3b).

The variances $\overline{\theta'^2_l}$ and $\overline{q'^2_t}$, and the covariance $\overline{q'_t\theta'_l}$ are shown in Fig. 5. Here, $\overline{\theta'^2_l}$ maximizes near cloud top with a variance of 0.14 K^2 at 1700 m for the RAMS LES and 0.08 K^2 at 1500 m for the SCM, reflecting again the lower cloud tops. The increase in variance with height below cloud top is slightly more gradual in the SCM than in the LES. Differences between the RAMS LES and SCM $\overline{q'_t\theta'_l}$ mirror those of $\overline{\theta'^2_l}$. Profiles of $\overline{q'^2_t}$ are comparable except near cloud base, where the LES predicts a large maximum in variance not present in the SCM model. The LES maximum is a reflection of the larger moisture gradient between the subcloud and cloud layers (Fig. 3b). Surprisingly, and in contrast to all the other moments shown previously, the SCM-generated moisture variance drops off at a higher elevation than it does in the LES. It is not clear why this happens. One hypothesis is that the relatively large moisture gradient between 1600 and 2000 m acts in conjunction with the residual total water flux in this layer to generate spurious total moisture variance through the production term $-2\overline{w'q'_t}(\partial\overline{q}_t/\partial z)$. This may not happen for $\overline{\theta'^2_l}$ because $\overline{w'\theta'_l}$ (not shown) is comparatively smaller than $\overline{w'q'_t}$ in the layer between 1600 and 2000 m.

The comparison of the LES and SCM results would not be complete without showing some examples of PDFs. PDFs from the RAMS LES and SCM as well as diagnostic PDF fits to the LES data are displayed in Fig. 6 for the last hour of the simulation. Two heights have been selected: near cloud base (z = 620 m) and in the middle of the cloud layer (z = 1020 m). Projections of the joint PDFs are shown on the w, θ_l, and q_t axes. The PDFs of w are positively skewed, with a long tail extending on the positive side of the distribution. The RAMS LES PDF has a tail extending up to 2 m s^{-1} at 620 m and up to 4 m s^{-1} at 1020 m. This long tail is characteristic of cumulus layers. The tail end is composed of the cloud cores, where the vertical velocity and moisture content are high. Because velocities in the core of the clouds increase with height, it is not surprising that the tail of the distribution is longer at 1020

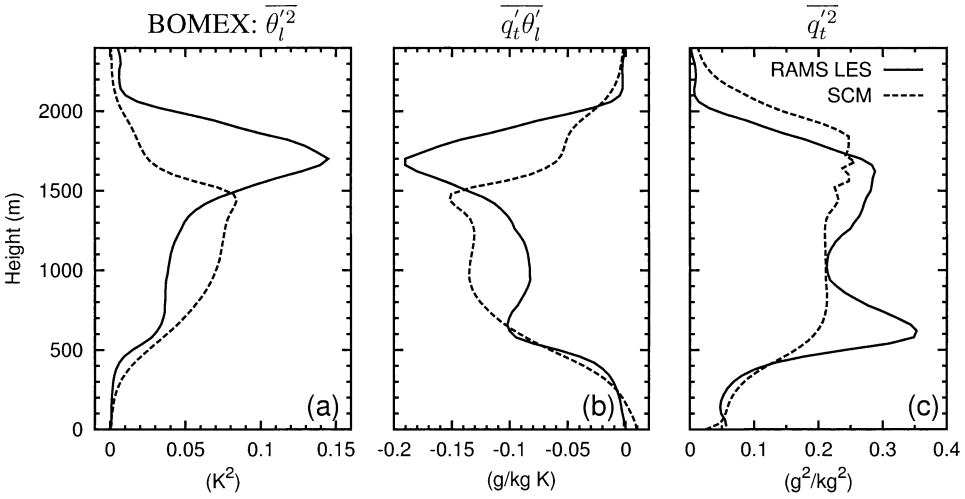

FIG. 5. Profiles of (a) $\overline{\theta_l'^2}$, (b) $\overline{q_t'\theta_l'}$ and (c) $\overline{q_t'^2}$ averaged over the last 3 h of the BOMEX simulation. Solid lines are RAMS LES results and dashed lines are SCM outputs.

m than at 620 m. The tail is captured by the SCM and the LES data, except that it is in both cases shorter than in the original distribution. For the PDFs of θ_l and q_t, the LES PDF diagnostic fit produces distributions that more closely resemble the original data, which is expected since the diagnostic PDF fit is based on the LES moments. The differences between the SCM and LES PDF reflect the mismatch of some of the SCM moments. For example, the SCM PDF of θ_l at $z = 1020$ m (Fig. 6d) is shifted to the left and is too broad. This is because at this height, the SCM predicts a lower mean (Fig. 3a) and a higher variance (Fig. 5a).

The mean state saturation specific humidity is shown along with the PDFs of q_t. It is the saturation value given by the layer-averaged $\overline{\theta}_l$ and $\overline{q}_t$ and provides an indication of where the distribution lies relative to the mean saturation. However, this does not imply that all the points to the right of the arrows are cloudy and the ones to the left are clear. This is because the saturation curve is a line on the θ_l and q_t plane [see for instance Figs. 1 and 2 in Larson et al. (2002)] which does not project onto a single point on the q_t axis. Nevertheless, the mean saturation provides useful information. At 620 m (Fig. 6e), a significant fraction of the distribution lies to the right of the mean saturation, whereas at 1020 m, a much smaller fraction does so (Fig. 6f), reflecting the decrease in cloud fraction between these levels. The PDF of q_t at 1020 m exhibits a long tail extending up to 17 g kg^{-1}, which is almost to the surface q_t value. This illustrates the fact that a portion of the air found in cloud cores has risen almost undiluted from the surface. The long q_t tail at 1020 m is captured quite realistically by the diagnostic PDF fit as well as the SCM.

4. Cumulus over land

In addition to the trade wind cumulus case, we also present results from continental cumulus clouds. The simulations are based on the sixth GCSS boundary layer clouds intercomparison workshop, which focused on a case of daytime, nonprecipitating cumulus clouds over land developing on top of an initially clear convective boundary layer. The case was idealized from observations taken at the Southern Great Plains (SGP) Atmospheric Radiation Measurement (ARM) site on 21 June 1997. A complete description of the intercomparison case can be found in Brown et al. (2002). We will only briefly outline some key features here. The models were initialized at 1130 UTC (530 LST) with profiles of potential temperature, total water mixing ratio, and horizontal winds derived from observed soundings at the ARM site. Time-varying surface latent and sensible heat fluxes derived from observations were used to force the models. Large-scale heat and moisture forcings intended to mimic advective and radiative forcings were also imposed, but no interactive radiation calculation was used. Results from the intercomparison workshop and a series of sensitivity experiments (Golaz et al. 2001) have shown that our LES compared favorably with other models and observations. Table 3 gives details of the model configuration.

Compared to BOMEX, domain-averaged cloud fraction and liquid water values here are larger, and the clouds are forced by a diurnally varying surface heating. As a result, the clouds exhibit a diurnal cycle, which allows us to test the timing of the onset and decay of the convection between the LES and the parameterization. This is shown in Fig. 7, which compares the time evolution of the cloud fraction for the RAMS LES and SCM. A 1-h running filter was applied to the LES cloud fraction because the instantaneous domain-averaged cloud fractions exhibited large intermittency on timescales shorter than 1 h. No such filtering was applied to the SCM results. Using the 1% contour line as a measure of the onset and decay of the convection, the

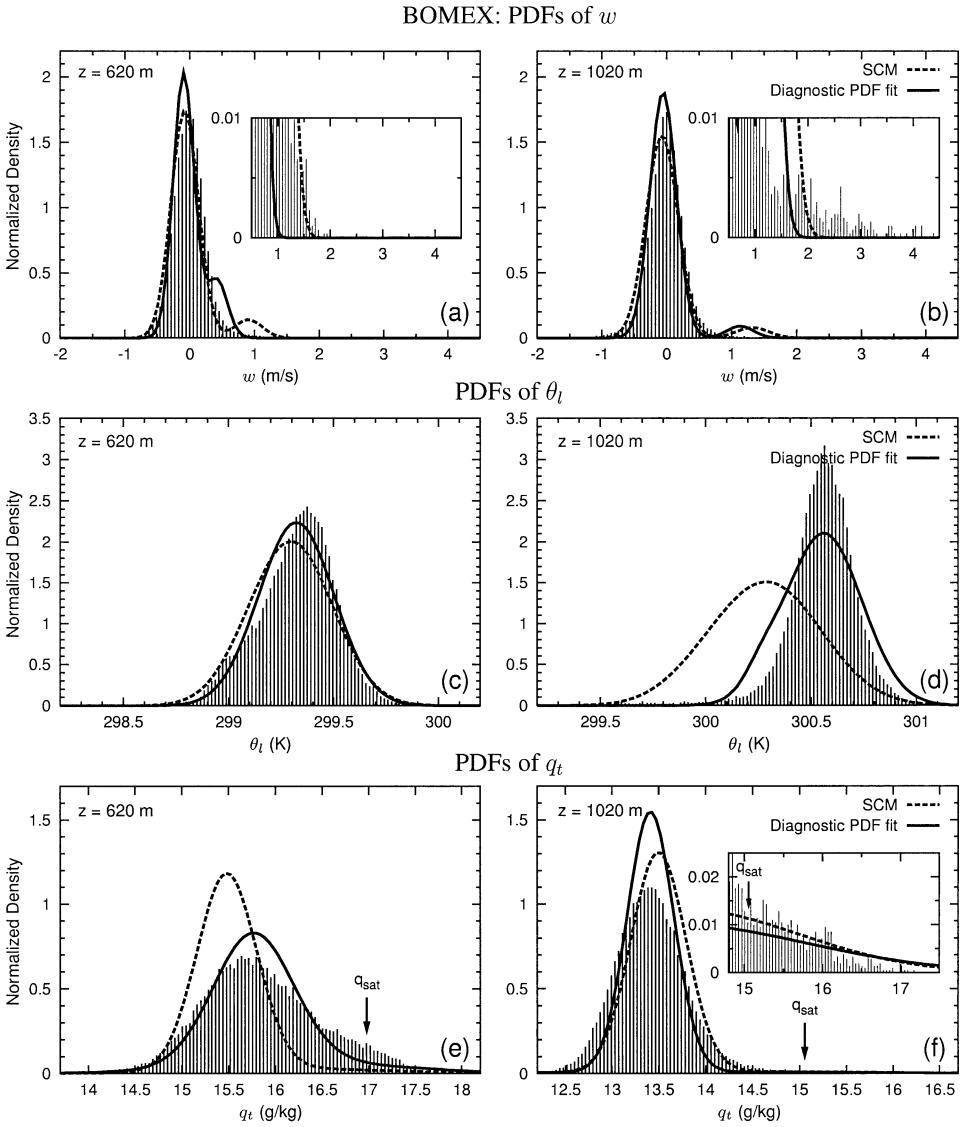

FIG. 6. Examples of PDFs of w, θ_l, and q_t over the last hour of the BOMEX simulation (a)–(f). Thin vertical lines show the actual RAMS LES distributions, thick dashed lines the PDFs predicted by the SCM, and thick solid lines the PDFs fit to the LES data. Vertical arrows in (e) and (f) indicate the mean state saturation specific humidity. Inserts show a close-up view of the tail of the distributions.

timing is very similar between the two models, with the first clouds appearing around 1530 UTC and the last ones dissipating around 0030 UTC. The evolution of cloud base during the course of the simulation is also in good agreement, with the main difference being a slightly lower cloud base in the SCM. Cloud top is also underestimated in the SCM by a few hundred meters. The RAMS LES produces a large maximum in cloud fraction of 18% around 1800 UTC. In comparison, the SCM produces a much smaller maximum value just over 10%, delayed by approximately 30 min and at a higher elevation. As we show later in the text, the parameterization tends, in general, to underestimate maximum cloud fraction for this case.

We now present profiles of various quantities averaged between 1900 and 2000 UTC, corresponding to the period when the surface heating is the strongest. Figures 8a,b depict $\overline{\theta}_l$ and $\overline{q}_t$ for both models during this time along with their initial values. The RAMS LES $\overline{\theta}_l$ increases in the lower part of the domain under the influence of surface heating, and there develops an approximately 1000-m-deep subcloud mixed layer. The mixing of subcloud layer air by the clouds causes $\overline{\theta}_l$ to decrease between 1100 and 2000 m. The RAMS LES humidity profile becomes moister throughout most of the domain, with the biggest increase in the subcloud layer as a result of the large surface latent heat flux. The SCM profiles at the same time are almost identical

TABLE 3. Model setup and forcings for the ARM case.

Model attribute	Forcing
Surface heat fluxes	Prescribed as a function of time based on observations.
Radiative cooling	Prescribed as a function of height
Large-scale advection	Prescribed as a function of height
Large-scale subsidence	None
Surface pressure	970 (hPa)
Start of simulation	1130 UTC 21 Jun 1997
Length of simulation	14.5 h
SCM:	
Time step	Main time step: 20 s; nested time step: 2.86 s
Grid spacing	$\Delta z = 40$ m
Domain size	$N_z = 110$
LES:	
Time step	Δt between 1 and 5 s
Grid spacing	$\Delta x = \Delta y = 100$ m; $\Delta z = 40$ m
Domain size	$N_x = N_y = 67$; $N_z = 110$
Case reference	Brown et al. (2002)

to the RAMS LES. This demonstrates that the SCM can realistically simulate the evolution of $\overline{\theta}_l$ and $\overline{q}_t$.

Cloud fraction and liquid water profiles for the same time period are shown in Figs. 8c,d. As was the case for BOMEX, the LES cloud fraction maximizes near cloud base and then decreases with height. The parameterization generates a similar shape, but with overall smaller cloud fraction values; the maximum is 8% compared to 12% for the RAMS LES. As in BOMEX, both cloud base and cloud top are underestimated, cloud base by approximately 100 m and cloud top by a larger amount of 200 to 300 m. The maximum amount of liquid water produced by the RAMS LES is approximately 0.028 g kg^{-1}, which is almost five times larger than in BOMEX. The SCM underestimates cloud water by 30%. It is encouraging to note that for both the BOMEX and ARM cases, the SCM model was capable of producing cloud water amounts within 30% of the RAMS LES, despite nearly a factor of five increase in overall liquid water. The differences in LWP are accentuated by the difference in cloud depth. The RAMS LES LWP is 22.04 g m^{-2} and the SCM value is 12.47 g m^{-2}, approximately 43% smaller.

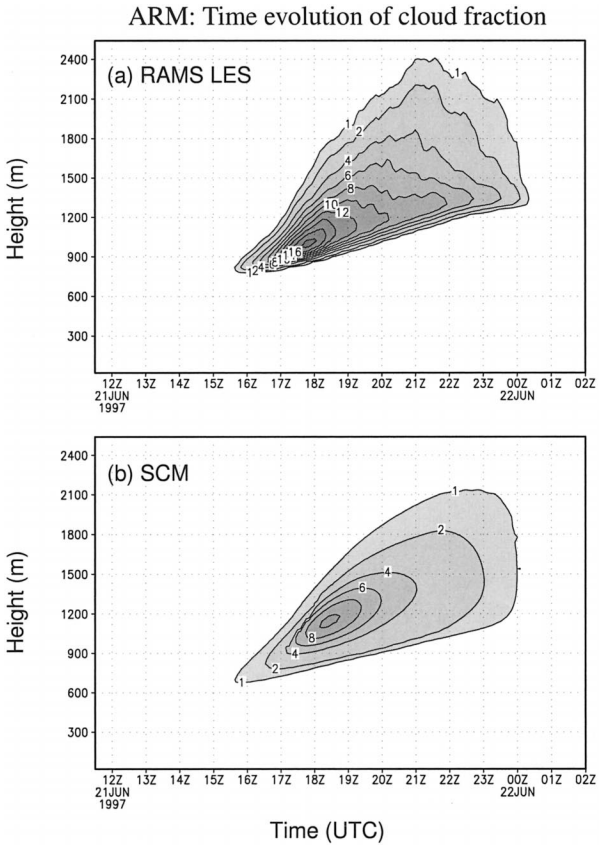

FIG. 7. Time evolution of the cloud fraction (%) produced by (a) the RAMS LES and (b) the SCM for the ARM case. A 60-min running average has been applied to the RAMS LES cloud fraction to smooth out intermittency.

Also shown in Figs. 8c,d are the diagnostic cloud properties obtained by fitting the family of PDFs to the RAMS LES moments. As was the case for BOMEX, cloud-base and cloud-top altitudes are also underestimated, which indicates that the family of PDFs is at least partially responsible for this underestimation in the SCM. However, the diagnosed magnitudes of cloud fraction and cloud water are much closer to the LES than to the SCM, thus pointing to a misprediction of the SCM moments as the most likely culprit for the lower SCM cloud amounts.

The vertical velocity variance profile ($\overline{w'^2}$; Fig. 9a) has a structure similar to BOMEX, with one maximum in the subcloud layer, another in the cloud layer, and a minimum near cloud base. However, the actual values are much larger reflecting more vigorous mixing due to the strong surface heating over land. The SCM variance is comparable to the RAMS LES except in the upper part of the domain where it drops off too rapidly, presumably because of the lower cloud top. The SCM sub

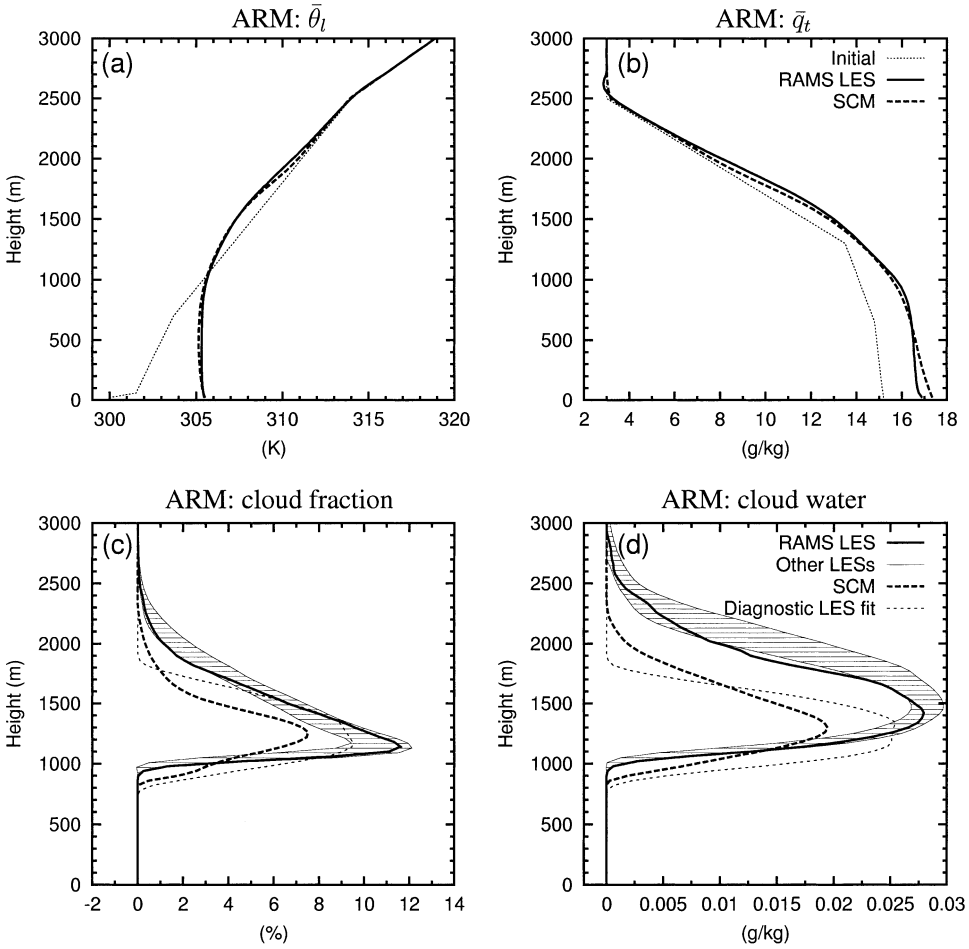

FIG. 8. Mean profiles of (a) liquid water potential temperature, (b) total water specific humidity, (c) cloud fraction, and (d) liquid water for the ARM case. Thick solid lines are RAMS LES results and the thick dashed line represents SCM results, both averaged between 1900 and 2000 UTC. Thin dotted lines in (a) and (b) represent initial profiles; thin dashed lines in (c) and (d) show cloud properties obtained using a diagnostic PDF fit to the LES data. The hatched regions in (c) and (d) represent twice the standard deviation around the mean of a suite of LES models (Brown et al. 2002).

cloud $\overline{w'^2}$ peak is too low compared to the LES, similar to Wangara. The $\overline{w'^3}$ profiles (Fig. 9b) are comparable with the exception of larger in-cloud values produced by the SCM. We will discuss this further when we present plots of PDFs of w. The difference in the buoyancy flux between the LES and the parameterization (Fig. 9c) is greatest in the cloud layer and is associated with the smaller SCM cloud water amount and the lower cloud top. The total water flux (Fig. 9d) is generally smaller in the parameterization, indicating a less vigorous mixing. Between the surface and 1500 m, the gradient of $\overline{w'q_t'}$ has different sign in the RAMS LES and the SCM. The RAMS LES gradient indicates a drying of this layer, whereas the SCM gives a slight moistening. When the cumulus activity is very strong, the clouds mix moisture out of the subcloud layer faster than the surface latent heat flux can replenish it, leading to a slight drying of the subcloud layer and a positive $\overline{w'q_t'}$ gradient. On the contrary, when the cumulus activity is weaker, the moisture in the subcloud layer is replenished by the surface flux, and the $\overline{w'q_t'}$ gradient is negative. The sign difference in the $\overline{w'q_t'}$ gradient in Fig. 9d therefore reflects the fact that the cumulus activity is weaker in the SCM than in the RAMS LES during the particular hour shown, which is consistent with the profiles of cloud fraction, liquid water, and $\overline{w'^2}$. One hour earlier, the RAMS LES $\overline{w'q_t'}$ gradient in the subcloud layer (not shown) is negative, reflecting a moistening of the layer.

The temperature and moisture variances and covariance (Fig. 10) are quite similar to BOMEX and so are the differences between the RAMS LES and the SCM. One notable difference with BOMEX is the absence of a local maximum in $\overline{q_t'^2}$ near cloud base. Such a maximum is not present in the ARM LES because the mean moisture profile (Fig. 8b) has a smaller gradient at cloud base compared to BOMEX (Fig. 3b).

Figure 11 shows examples of PDFs near cloud base (z = 1060 m) and higher in the cloud (z = 1660 m).

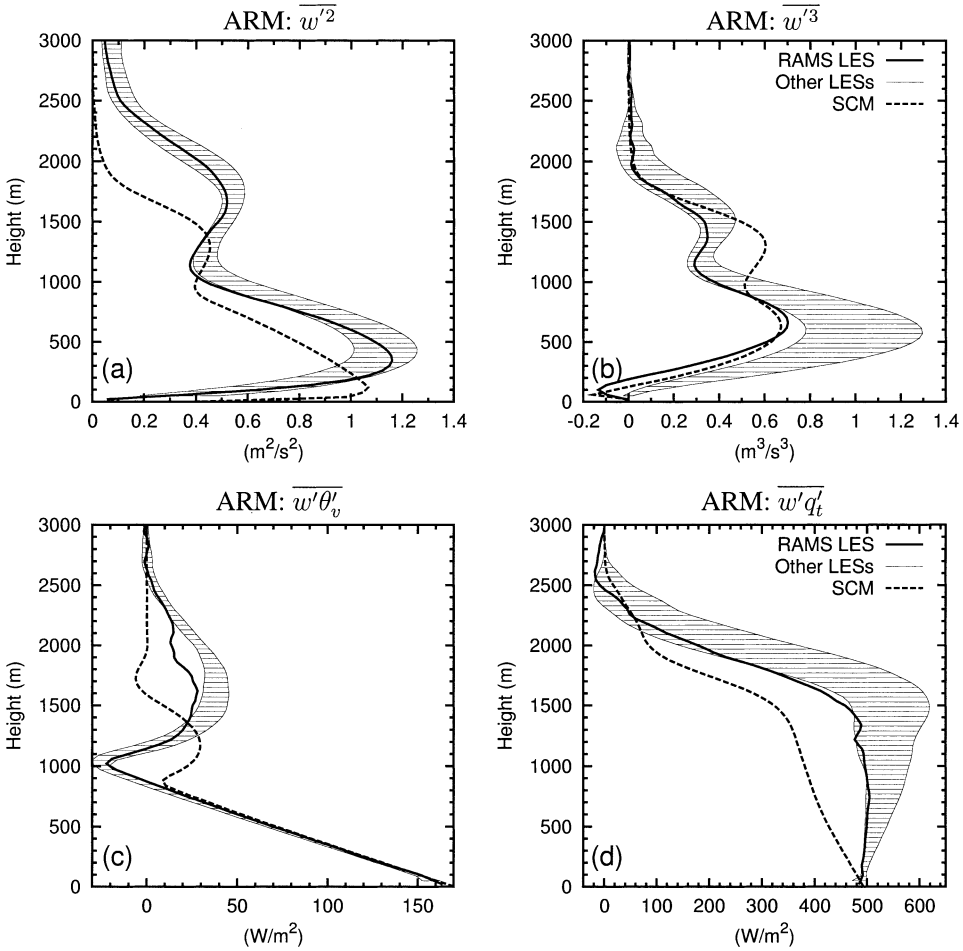

FIG. 9. Profiles of (a) $\overline{w'^2}$, (b) $\overline{w'^3}$, (c) $\overline{w'\theta_v'}$, and (d) $\overline{w'q_t'}$, averaged between 1900 and 2000 UTC of the ARM simulation. Solid lines are RAMS LES results and dashed lines are SCM outputs. The hatched regions represent twice the standard deviation around the mean of a suite of LES models (Brown et al. 2002).

In many respects, those PDFs are similar to BOMEX. The RAMS LES PDFs of w have long tails, extending to nearly 4 m s^{-1} at cloud base, and 6 m s^{-1} in the middle of the cloud. The longer tail at 1660 m is due to the fact that w in the cloud cores increases between 1060 and 1660 m. The SCM and LES PDF fits produce positive tails, but they are shorter than in the original data. Interestingly, the SCM tails are longer than the diagnostic PDF fit, and therefore slightly more realistic. This is because the SCM overpredicts $\overline{w'^3}$ between 1000 and 1600 (Fig. 9b), and thus the tail of the resulting PDF is longer. The θ_l distribution at 1060 m (Fig. 11c) is nearly symmetrical with a Gaussian-like form. Both the SCM and the PDF fits represent it well, illustrating that the analytic double Gaussian 1 family of PDFs can reduce to a nearly single Gaussian shape. At higher elevation (Fig. 11d), the distribution has a long negative tail. It is not captured well by either the SCM or the PDF fit because the family of PDFs used does not require the θ_l skewness of the fitted distribution to match the skewness of the underlying data. In the upper portion of the cloud, the PDF of q_t exhibits a long positive tail (Fig. 11f) formed by the cloud cores. The maximum specific humidity value in this tail (17 g kg^{-1}) is similar to the mean surface value (Fig. 8b). The diagnostic PDF fit captures the tail quite nicely, but the SCM underestimates the magnitude.

5. Stratocumulus

Lastly, we present results from a case of nocturnal stratocumulus clouds based on the first GCSS boundary layer clouds intercomparison workshop. Detailed description of the case and analysis of LES output are given in Moeng et al. (1996). Intercomparisons between one-dimensional codes and LESs are presented in Bechtold et al. (1996). Initial model soundings were loosely based on observations from the First International Satellite Cloud Climatology Project (ISCCP) Regional Experiment (FIRE) nearly solid cloud case on 7 July 1987. The idealized case is during nighttime with no drizzle, no solar radiation, little wind shear and little

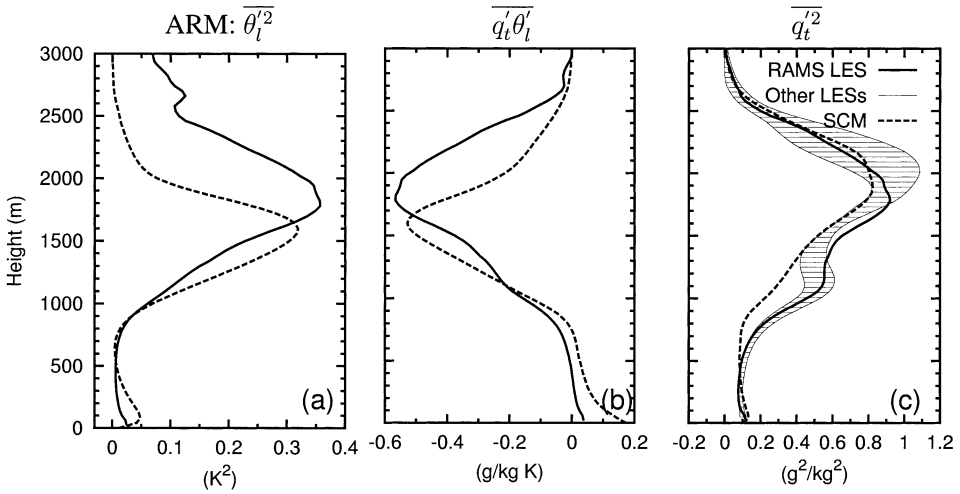

FIG. 10. Profiles of (a) $\overline{\theta_l'^2}$, (b) $\overline{q_t'\theta_l'}$, and (c) $\overline{q_t'^2}$ averaged between 1900 and 2000 UTC of the ARM simulation. Solid lines are RAMS LES results and dashed lines are SCM outputs. The hatched regions in (c) represent twice the standard deviation around the mean of a suite of LES models (Brown et al. 2002).

surface heating. Turbulence in the boundary layer is mainly generated by longwave cooling at cloud top. A very simple longwave radiative transfer model, based on liquid water path, is used:

$$F_{\text{rad}}(z) = F_0 \exp\left[-\kappa \int_0^{\infty} \rho(z')q_l(z')\, dz'\right], \qquad (4)$$

where ρ is the basic-state density and q_l the liquid water. The constants are $F_0 = 74$ W m^{-2} and $\kappa = 130$ m kg^{-1}. Similar simple radiative models have been used successfully in other intercomparison studies (e.g., Bretherton et al. 1999; Stevens et al. 2001). Other details of the simulation setup are given in Table 4.

The models were integrated for a total of 3 h and the results shown are averaged over the last hour of the simulation. Figures 12a,b compare $\overline{\theta}_l$ and $\overline{q}_t$ from the RAMS LES and the SCM. Differences between the two appear mostly near the inversion region; the SCM produces an inversion in both $\overline{\theta}_l$ and $\overline{q}_t$ that is slightly smoothed out compared to that of the LES. The height of the inversion is also slightly lower in the parameterization, indicating a smaller entrainment rate. Consequences of these inversion layer differences can be seen on the plots of cloud fraction and water (Figs. 12c,d). The cloud fraction profiles, although very similar in shape and magnitude between the two models, appears to be shifted downward by 50 m for the parameterization. The smoother SCM inversion also leads to 40% less maximum liquid water. Because the SCM's inversion is smoother, there is less total water available just below the inversion than in the LES (Fig. 12b), and therefore not as much condensed water. As a result, the LWP in the SCM (21.23 g m^{-2}) is also smaller than in the LES (33.57 g m^{-2}).

Cloud properties diagnosed by fitting the family of PDFs directly to the LES moments are almost identical to the LES cloud profiles (Figs. 12c,d). This indicates that, to first order, the discrepancies in cloud fraction and liquid water between the SCM and the LES result from the poor prediction of certain moments by the SCM and not from the family of PDFs. However, the family of PDFs might play a secondary role if it is responsible for the poor prediction of these moments. Other possible factors leading to errors in the SCM moments include the damping terms or the numerical discretization of the predictive equations across the inversion layer. Because of the strong and complicated interaction between the PDF closure and the 10 prognostic equations, it is unfortunately not clear to us if one factor in particular or a combination of factors is responsible for the misprediction of the moments.

Profiles of the turbulent quantities $\overline{w'^2}$ and $\overline{w'^3}$ are shown in Figs. 13a,b. They are very different from the cumulus cloud layers and exhibit a large maximum near cloud top caused by the generation of turbulence by longwave radiative cooling. Here, $\overline{w'^2}$ is similar between the LES and SCM, except that the magnitude is generally smaller in the SCM. The secondary maximum in the LES above the inversion is related to wave activity in the stable layer. The LES $\overline{w'^3}$ is small compared to the cumulus cases because stratocumulus layers typically have little skewness. It is also negative throughout the entire boundary layer, which corresponds to relatively few and narrow downdrafts as one would expect for turbulence driven by cloud-topped cooling. Here, $\overline{w'^3}$ is very different in the SCM. Negative values are only produced near the surface, and most of the layer has positive skewness with an unrealistic maximum in $\overline{w'^3}$ just below cloud top. However, this discrepancy does not seem to degrade the overall simulation very much, possibly because skewness values in stratocumulus layers tend to be relatively small.

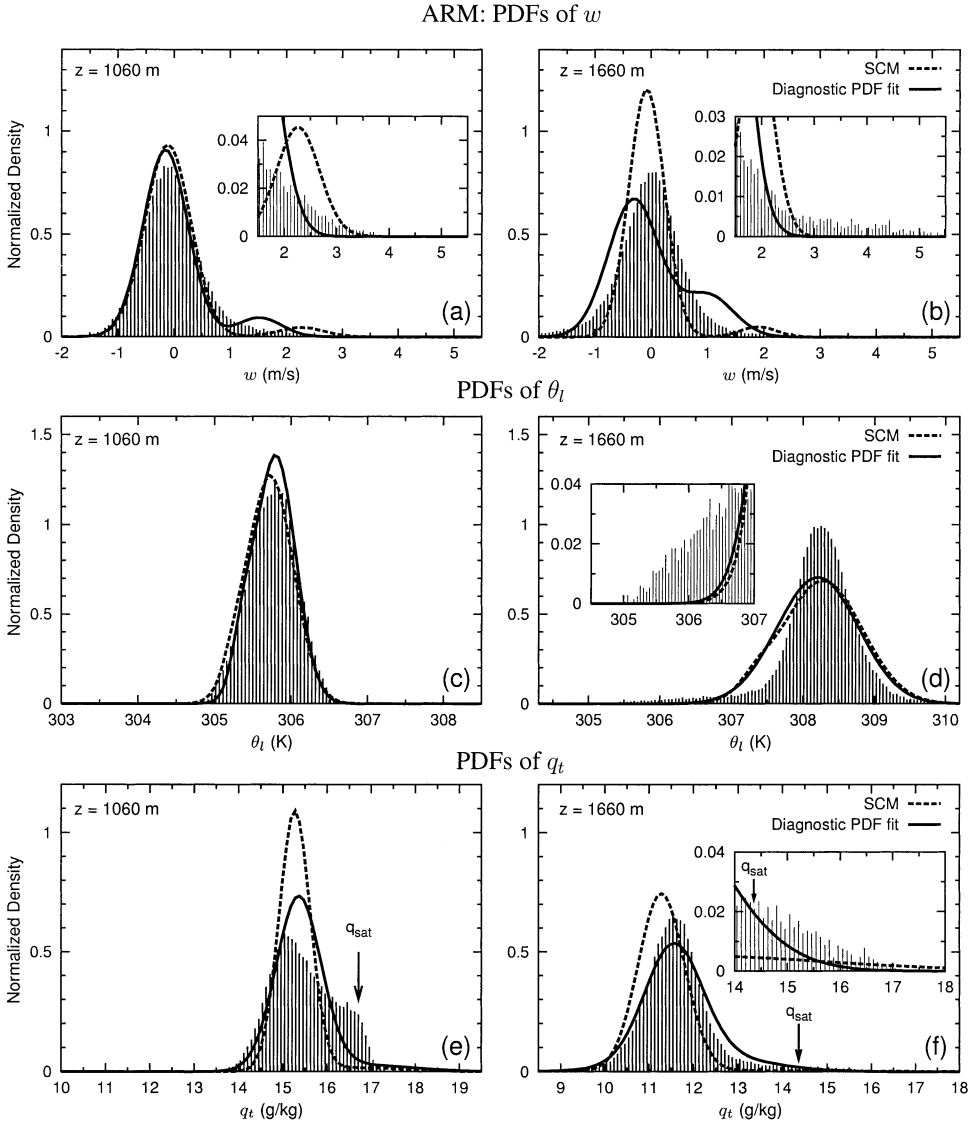

FIG. 11. Examples of PDFs of w, θ_l, and q_t between 1900 and 2000 UTC of the ARM simulation (a)–(f). Thin vertical lines show the actual RAMS LES distributions, thick dashed lines the PDFs predicted by the SCM, and thick solid lines the PDFs fit to the LES data. Vertical arrows in (e) and (f) indicate the mean state saturation specific humidity. Inserts show a close-up view of the tail of the distributions.

The turbulent buoyancy and total water fluxes are depicted in Figs. 13c,d. The buoyancy flux peaks near cloud top. The SCM flux is slightly larger in the subcloud layer, but comparable in the cloud layer. The LES produces a larger value of total water flux throughout most of the boundary layer. The variances $\overline{\theta_l'^2}$ and $\overline{q_t'^2}$ as well as the covariance $\overline{q_t'\theta_l'}$ (Fig. 14) produced by the SCM are much smaller than the ones from the LES. This is because the turbulent production terms $\overline{w'\theta_l'}\partial\overline{\theta}_l/\partial z$ and $\overline{w'q_t'}\partial\overline{q}_t/\partial z$ appearing in the prognostic equations for $\overline{\theta_l'^2}$, $\overline{q_t'^2}$, and $\overline{q_t'\theta_l'}$ are much smaller. This, in turn, is because the SCM-predicted inversion is much smoother, and hence the gradients of $\overline{\theta}_l$ and $\overline{q}_t$ at cloud top are much smaller.

Finally, Figure 15 shows some PDFs at 662 m (lower part of the cloud) and 787.5 m (just below LES cloud top). The LES PDFs are very different from the PDFs of cumulus layers. At 662 m, they have little skewness and tend to be narrow. The PDF of w extends from -1.5 to 1.5 m s^{-1}, reflecting the smaller vertical velocities commonly observed in stratocumulus clouds. The spread is also much smaller along the θ_l and q_t axes than in cumulus layers. However, the picture is strikingly different just below LES cloud top. There, the PDF of w is even narrower, spanning a range of under 1 m s^{-1}, whereas the PDFs of temperature and moisture become extremely broad. This broadening results from two related factors: the entrainment of air from above

TABLE 4. Model setup and forcings for the FIRE case.

Model attribute	Forcing
Surface heat fluxes	Bulk aerodynamic formulas; SST = 288 K
Radiative cooling	LW based on LWP [Eq. (4)]; no SW radiation
Large-scale advection	None
Large-scale subsidence	Imposed divergence of 5×10^{-6} s^{-1}
Surface pressure	1000 (hPa)
Length of simulation	3 h
SCM:	
Time step	Main time step: 6 s; nested time step: 1.2 s
Grid spacing	$\Delta z = 25$ m
Domain size	$N_z = 50$
LES:	
Time step	$\Delta t = 2$ s
Grid spacing	$\Delta x = \Delta y = 50$ m; $\Delta z = 25$ m
Domain size	$N_z = N_y = 60$; $N_z = 48$
Case reference	Moeng et al. (1996); Bechtold et al. (1996)

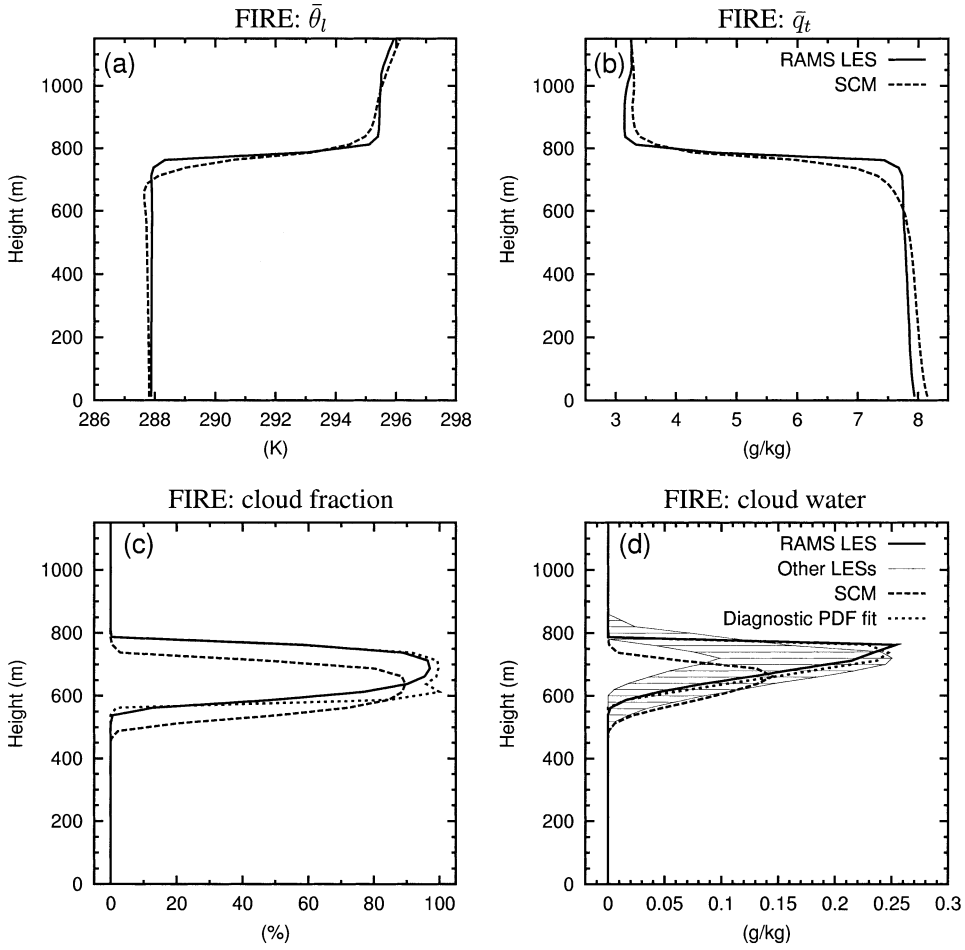

FIG. 12. Mean profiles of (a) liquid water potential temperature, (b) total water specific humidity, (c) cloud fraction, and (d) liquid water for the FIRE case. Thick solid lines RAMS LES results and thick dashed line SCM results, both averaged over the last hour of the simulation. Dotted lines in (c) and (d) show cloud properties obtained using a diagnostic PDF fit to the LES data. The hatched region in panel (d) shows the spread of LES models from the intercomparison workshop (Moeng et al. 1996).

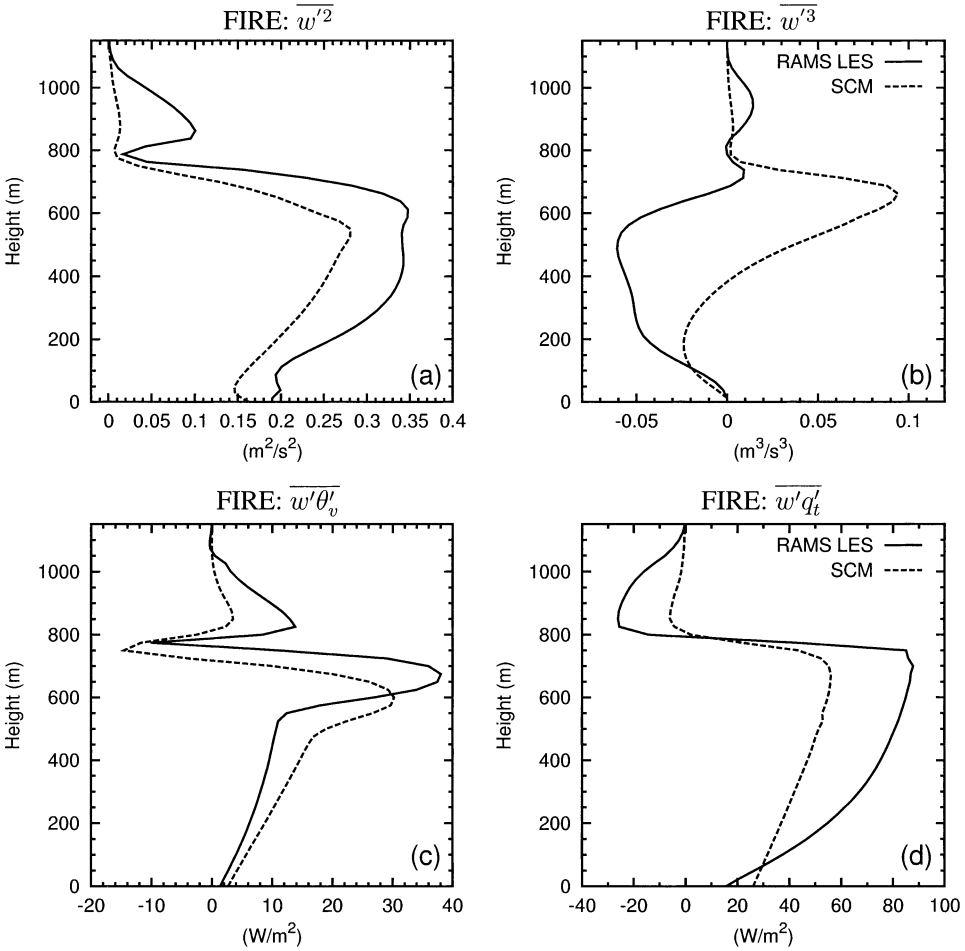

FIG. 13. Profiles of (a) $\overline{w'^2}$, (b) $\overline{w'^3}$, (c) $\overline{w'\theta'_v}$, (d) $\overline{w'q'_t}$ for the last hour of FIRE case. Solid lines are RAMS LES results and dashed lines are SCM outputs. The subgrid-scale contribution is included in the LES $\overline{w'^2}$ profile.

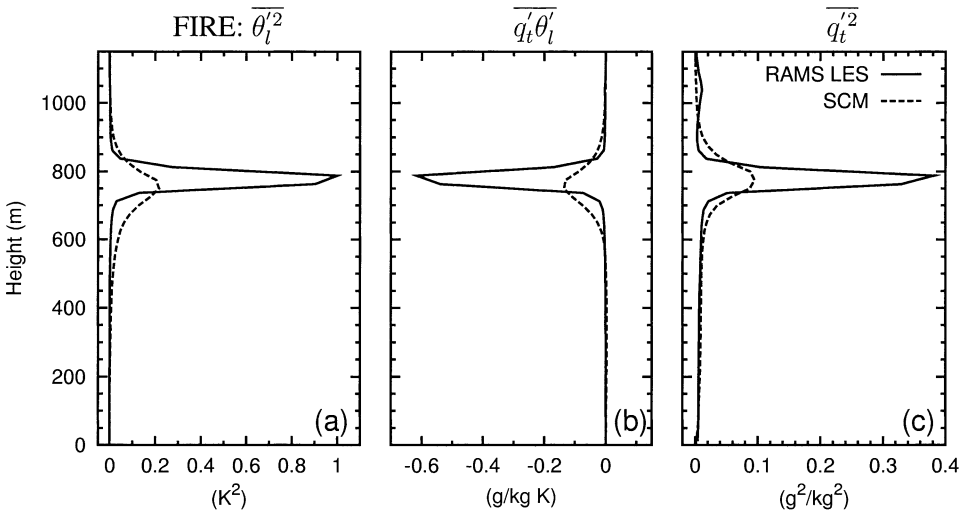

FIG. 14. Profiles of (a) $\overline{\theta'^2_l}$, (b) $\overline{q'_t\theta'_l}$, and (c) $\overline{q'^2_t}$ averaged over the last hour of the FIRE simulation. Solid lines are RAMS LES results and dashed lines are SCM outputs.

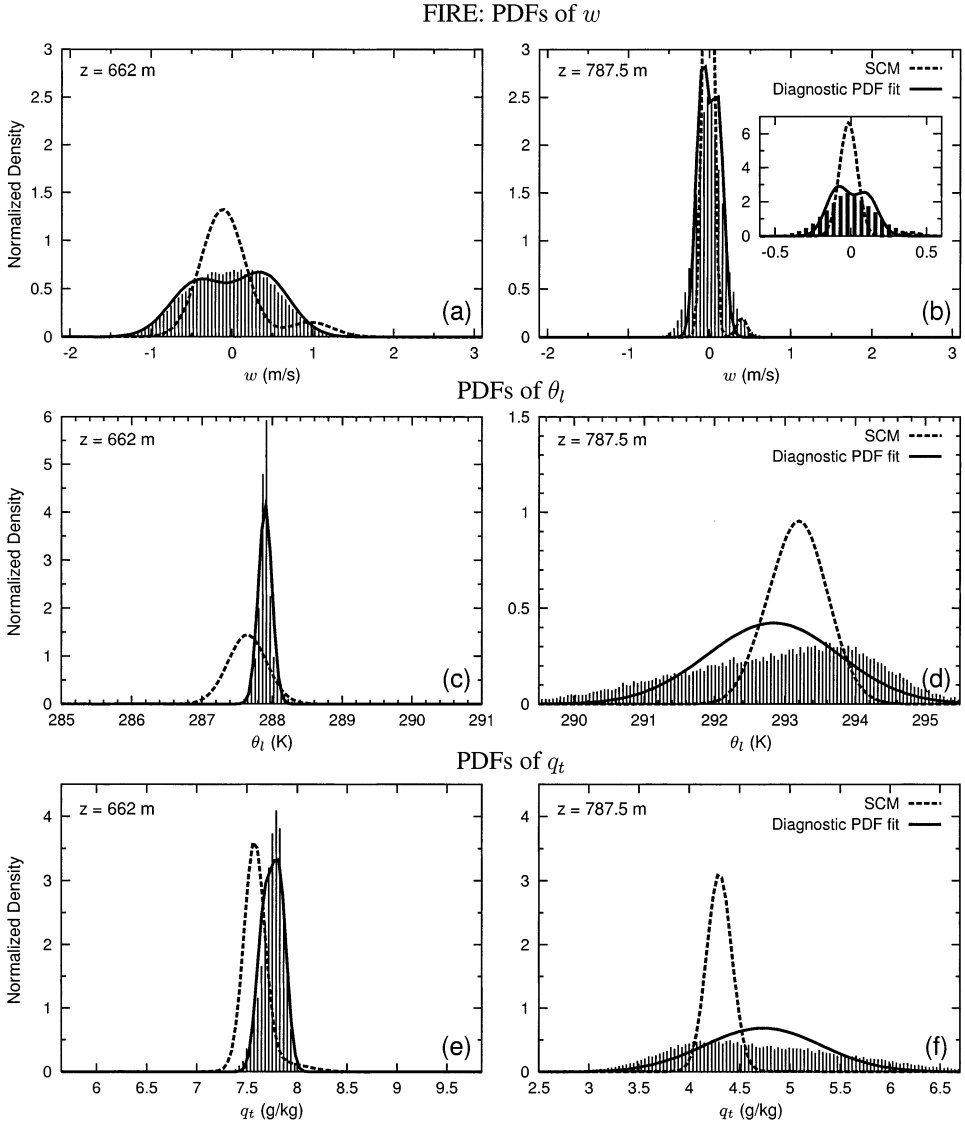

FIG. 15. Examples of PDFs of w, θ_l, and q_t over the last hour of the FIRE simulation (a)–(f). Thin vertical lines show the actual RAMS LES distributions, thick dashed lines the PDFs predicted by the SCM, and thick solid lines the PDFs fit to the LES data. Insert on (b) shows full extent of the SCM PDF.

the inversion into the cloud layer, and the fact that the inversion top varies in altitude throughout the horizontal layer near cloud top. The PDF at 787.5 m therefore samples two air masses with very distinct characteristics. Overall, the diagnostic PDF fit produces reasonable fits to the underlying LES data at both heights. This shows that the family of PDFs is flexible enough to fit relatively unskewed data. Because the SCM does not predict $\overline{w'^3}$ very accurately in the cloud layer, the SCM PDF of w at 662 m has a different shape from the LES. The SCM PDF of θ_l at the same height is too broad and shifted to the left. It is too broad because the SCM variance at this altitude is too large (Fig. 14a), and it is shifted to the left because the $\overline{\theta}_l$ is slightly smaller than the LES (Fig. 12a). The SCM PDF of q_t at 662 m looks better, except that it is centered at a lower moisture value due to the smaller SCM $\overline{q}_t$. The SCM PDFs at 787.5 m are very different from the LES. This is not surprising since the SCM variances are much smaller at this level than in the LES (Fig. 14). The SCM inversion is not as sharply defined in the vertical, resulting in much smaller variances and hence narrower PDFs.

6. Sensitivity to vertical grid spacing

Finally, we briefly explore the sensitivity to vertical grid spacing by showing sample results of SCM simulations with finer and coarser grid spacing. We do so for the BOMEX and the FIRE cases because they represent very different cloud regimes. The BOMEX case

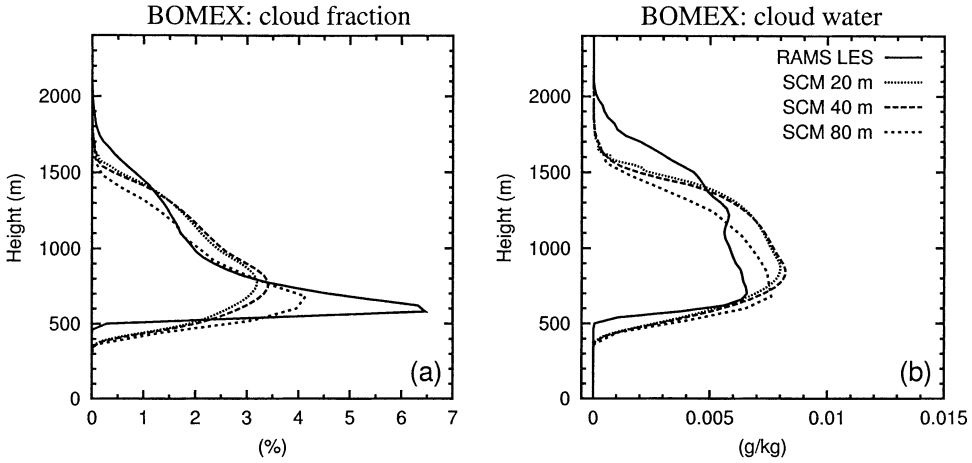

FIG. 16. Profiles of (a) cloud fraction, and (b) cloud water for the BOMEX case. Solid lines are RAMS LES results, dotted lines are SCM outputs with 20-m vertical grid spacing, long dashed lines are SCM with 40-m grid spacing, and short dashed lines are SCM with 80-m grid spacing.

is run with a grid increment that is halved (20 m) and doubled (80 m) from its original value (40 m). A main time step of 37.5 s is sufficient for the 80-m run, compared to the 20-s time step used for the 40-m run. Three additional simulations are performed for the FIRE case, one with half (12.5 m), one with double (50 m), and one with triple (75 m) grid spacing. The main time step for the 50 and 75 m is increased to 30 s, considerably longer than the 6-s time step used for the 25-m run.

Figure 16 depicts the cloud fraction and liquid water for the BOMEX case. The differences between the 40-m and 20-m runs are extremely small, indicating that the model has essentially converged at 40-m grid spacing and that no improvement is gained by further refinement of the vertical resolution. The differences between the 40-m and 80-m SCM simulations are rather small. The maximum value of cloud fraction is actually slightly better with the 80-m than the 40-m grid spacing, but cloud top is lower with the coarser resolution. Liquid water profiles are similar, with the main difference being the lower cloud top.

The results for the nighttime stratocumulus case are shown in Fig. 17. As for BOMEX, the results obtained at the standard (25 m) and the reduced spacing (12.5 m) are essentially identical. Compared to the 25-m grid spacing simulation, the 50-m run is slightly degraded and produces smaller cloud fraction and cloud water values. The maximum cloud fraction is approximately 85% compared to 90%, and the maximum liquid water 0.11 g kg^{-1} compared to 0.15 g kg^{-1}. The 75-m grid spacing run exhibits further degradation. Even though the maximum cloud fraction and liquid water values are comparable to the 50-m run, the shapes of the profiles become quite different and much less stratocumulus-like.

Overall, it appears that moderate changes from the standard grid spacing do not lead to different or improved results. A doubling of the vertical grid spacing still yields results with reasonable cloud properties. However, when the vertical grid spacing is further increased, the results degrade rapidly due to the model's inability to accurately resolve important features, such as the presence of an inversion layer. To obtain reasonable cloud properties when the grid spacing exceeds 50 to 80 m, the parameterization would need to be modified. One possible approach might be to modify the numerical discretization in order to reconstruct inversions, as proposed by Grenier and Bretherton (2001).

7. Summary and conclusions

The new SCM, which is based on a PDF closure, was tested for a variety of boundary layer regimes and was found to be capable of producing reasonable results without the need for any case-specific adjustments. The four cases were a clear convective layer, a trade wind cumulus regime, a continental cumulus layer, and a nighttime marine stratocumulus layer.

For the clear convective layer, the SCM produced a reasonable time evolution of the boundary layer growth, although the mixed layer was slightly less well mixed than in the LES.

For the trade wind cumulus layer, the SCM produced a maximum cloud fraction of 3.5% compared to 6% for the LES, and cloud water was approximately 30% larger than in the LES. Cloud base was underestimated by 100 m and cloud top by a few hundred meters.

The continental cumulus case differed from the trade wind case in that it exhibited a diurnal cycle, with the cumulus clouds forming on top of a previously clear convective layer and dissipating before sunset. The timing of the onset and decay of the clouds was well captured by the SCM. The daytime evolution of the mean temperature and moisture profiles was also represented accurately. Cloud fraction and liquid water were slightly smaller in the SCM. As for the trade wind cumulus case,

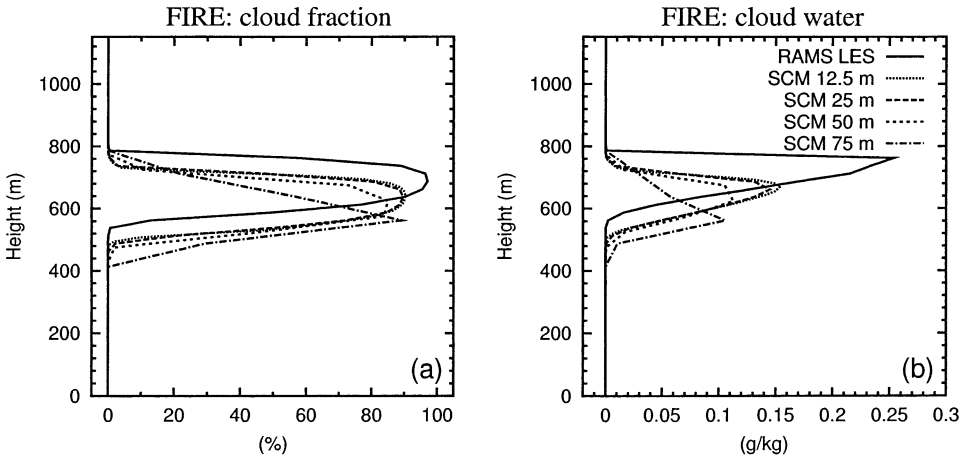

FIG. 17. Profiles of (a) cloud fraction, and (b) cloud water for the FIRE case. Solid lines are RAMS LES results, dotted lines are SCM outputs with 12.5-m vertical grid spacing, long dashed lines are SCM with 25-m grid spacing, short dashed lines are SCM with 50-m grid spacing, and dashed–dotted lines are SCM with 75-m grid spacing.

cloud-base and cloud-top altitudes were underestimated by the SCM.

The last case was a nocturnal stratocumulus-topped boundary layer with much larger cloud fraction and liquid water. Cloud fraction was almost identical between the SCM and the LES, but maximum liquid water at cloud top was 40% lower in the SCM. This was probably because the capping inversion was smoother in the SCM than in the LES, thereby reducing the amount of total water available near cloud top.

Overall, the layer-averaged liquid water content produced by the SCM was typically within 40% of the LES for all the cloudy cases. This is encouraging because the liquid water values ranged from 0.006 to 0.3 g kg^{-1}.

We believe that this work demonstrates some of the potential of the assumed PDF method. If a parameterization is based upon a sufficiently realistic and flexible family of PDFs, then it can represent various regimes without the need for case-specific adjustments or trigger functions that switch between regimes. The PDF approach also offers a framework in which cloud properties, turbulence, and buoyancy moments can all be diagnosed directly from the PDF, and therefore are guaranteed to be consistent with each other. The main disadvantages of the method are related to its computational costs. For instance, to obtain the PDF parameters, additional prognostic moment equations are needed. These additional equations tend to degrade the numerical stability and limit the maximum allowable time step. Also, in the current implementation of the PDF method, inversions must be explicitly resolved, and therefore a relatively fine vertical grid spacing is needed.

We hope to address some of these shortcomings in the future by simplifying the method and reducing its cost. More test cases would also be useful. We have simulated a mixed case consisting of cumulus clouds rising into a broken stratocumulus (Stevens et al. 2001) and found that the SCM was capable of representing quite realistically the simultaneous presence of the two regimes (Golaz 2001). Future extensions could include exploring the feasibility of using the PDF method for different cloud regimes, such as Arctic boundary layer clouds, midlevel clouds, and even deep convection. Furthermore, the knowledge of the subgrid-scale PDF could also be used to reduce biases that arise due to the neglect of subgrid scale variability in certain microphysical processes (Larson et al. 2001).

Finally, the true value of the PDF method will only be known if the scheme is implemented and tested in a full-physics large-scale model. We believe that future refinements of the PDF method could reduce its computational cost enough to render it of practical use in upcoming mesoscale models. We hope that a PDF-based parameterization is implemented in such a model in the future.

Acknowledgments. We are especially thankful to Cara-Lyn Lappen for reading and suggesting improvements to this manuscript, and to Andy Brown and Pier Siebesma for making LES data from the intercomparison workshops available. We are also grateful to three anonymous reviewers for their valuable comments and suggestions. J.-C. Golaz and W. R. Cotton were supported by the National Science Foundation under Grants ATM-9529321 and ATM-9904218. V. E. Larson was supported by the National Oceanic and Atmospheric Administration under Contract NA67RJ0152.

REFERENCES

André, J. C., G. de Moor, P. Lacarrère, G. Therry, and R. du Vachat, 1978: Modeling the 24-hour evolution of the mean and turbulent structures of the planetary boundary layer. *J. Atmos. Sci.*, **35,** 1861–1883.

Bechtold, P., S. K. Krueger, W. S. Lewellen, E. van Meijgaard, C.-

H. Moeng, D. A. Randall, A. van Ulden, and S. Wang, 1996: Modeling a stratocumulus-topped PBL: Intercomparison among different one-dimensional codes and with large eddy simulation. *Bull. Amer. Meteor. Soc.,* **77,** 2033–2042.

Bretherton, C. S., and Coauthors, 1999: An intercomparison of radiatively driven entrainment and turbulence in a smoke cloud, as simulated by different numerical models. *Quart. J. Roy. Meteor. Soc.,* **125,** 391–423.

Brown, A. R., and Coauthors, 2002: Large-eddy simulation of the diurnal cycle of shallow cumulus convection over land. *Quart. J. Roy. Meteor. Soc.,* **128,** 1075–1094.

Clarke, R. H., A. J. Dyer, R. R. Brook, D. G. Reid, and A. J. Troup, 1971: The Wangara experiment: Boundary layer data. Tech. Paper 19, Division of Meteorological Physics, CSIRO, Australia.

Cotton, W. R., and Coauthors, 2002: RAMS 2001: Current status and future directions. *Meteor. Atmos. Phys.,* in press.

Deardorff, J. W., 1966: The counter-gradient heat flux in the lower atmosphere and in the laboratory. *J. Atmos. Sci.,* **23,** 503–506.

——, 1974: Three-dimensional numerical study of the height and mean structure of a heated planetary boundary layer. *Bound.-Layer Meteor.,* **7,** 81–106.

——, 1980: Stratocumulus-capped mixed layers derived from a three-dimensional model. *Bound.-Layer Meteor.,* **18,** 495–527.

Ebert, E. E., U. Schumann, and R. B. Stull, 1989: Nonlocal turbulent mixing in the convective boundary layer evaluated from large-eddy simulation. *J. Atmos. Sci.,* **46,** 2178–2207.

Golaz, J.-C., 2001: A PDF-based parameterization for boundary layer clouds. Ph.D. dissertation, Dept. of Atmospheric Science, Colorado State University, 124 pp.

——, H. Jiang, and W. R. Cotton, 2001: A large-eddy simulation study of cumulus clouds over land and sensitivity to soil moisture. *Atmos. Res.,* **59–60,** 373–392.

——, V. E. Larson, and W. R. Cotton, 2002: A PDF-based model for boundary layer clouds. Part I: Method and model description. *J. Atmos. Sci.,* **59,** 3540–3551.

Grenier, H., and C. S. Bretherton, 2001: A moist PBL parameterization for large-scale models and its application to subtropical cloud-topped marine boundary layers. *Mon. Wea. Rev.,* **129,** 357–377.

Holland, J. Z., and E. M. Rasmusson, 1973: Measurement of atmospheric mass, energy and momentum budgets over a 500-kilometer square of tropical ocean. *Mon. Wea. Rev.,* **101,** 44–55.

Lappen, C.-L., and D. A. Randall, 2001a: Toward a unified parameterization of the boundary layer and moist convection. Part II: Lateral mass exchanges and subplume-scale fluxes. *J. Atmos. Sci.,* **58,** 2037–2051.

——, and ——, 2001b: Toward a unified parameterization of the boundary layer and moist convection. Part III: Simulations of clear and cloudy convection. *J. Atmos. Sci.,* **58,** 2052–2072.

Larson, V. E., R. Wood, P. R. Field, J.-C. Golaz, T. H. Vonder Haar, and W. R. Cotton, 2001: Systematic biases in the microphysics and thermodynamics of numerical models that ignore subgrid-scale variability. *J. Atmos. Sci.,* **58,** 1117–1128.

——, J.-C. Golaz, and W. R. Cotton, 2002: Small-scale and mesoscale variability in cloudy boundary layers: Joint probability density functions. *J. Atmos. Sci.,* **59,** 3519–3539.

Lenschow, D. H., J. C. Wyngaard, and W. T. Pennell, 1980: Mean-field and second-moment budgets in a baroclinic, convective boundary layer. *J. Atmos. Sci.,* **37,** 1313–1326.

Moeng, C.-H., and Coauthors, 1996: Simulation of a stratocumulus-topped planetary boundary layer: Intercomparison among different numerical codes. *Bull. Amer. Meteor. Soc.,* **77,** 261–278.

Pielke, R. A., and Coauthors, 1992: A comprehensive meteorological modeling system—RAMS. *Meteor. Atmos. Phys.,* **49,** 69–91.

Siebesma, A. P., and J. W. M. Cuijpers, 1995: Evaluation of parametric assumptions for shallow cumulus convection. *J. Atmos. Sci.,* **52,** 650–666.

Stevens, B., and Coauthors, 2001: Simulations of trade wind cumuli under a strong inversion. *J. Atmos. Sci.,* **58,** 1870–1891.

Stull, R. B., 1988: *An Introduction to Boundary Layer Meteorology.* Kluwer Academic, 666 pp.